PAPER

Preparation of carbon coated MoS₂ flower-like nanostructure with self-assembled nanosheets as high-performance lithium-ion battery anodes†

Shan Hu,[ab] Wen Chen,*[a] Jing Zhou,[a] Fei Yin,[c] Evan Uchaker,[b] Qifeng Zhang[b] and Guozhong Cao*[b]

Loosely packed MoS₂ nanosheets with thin carbon coating were synthesized *via* a facile, one-pot hydrothermal growth method. In the resulting optimally-designed nanoarchitecture, the ultrathin nanosheets, with a wall-thickness of approximately 5–10 nm, provide a large electrode–electrolyte interface so as to facilitate faster lithium-ion intercalation and diffusion. The flexible and conductive carbon overcoats stabilize the disordered structure of flower-like MoS₂ nanosheets to accommodate more lithium-ions intercalation and thus maintain the structural and electrical integrity during cycling processes. In favor of the synergy and interplay of the carbon effect and intrinsic structural advantages, C@MoS₂ (2 : 1) composites synthesized with a D-glucose precursor: MoO₃ molar ratio of 2 : 1 exhibit high reversible specific capacity of 1419 mA h g⁻¹ at 0.1 A g⁻¹, retain 80% of the capacity after 50 cycles, and excellent rate capability as high as 672 mA h g⁻¹ at 10 A g⁻¹ with nearly 100% coulombic efficiency. The good electrochemical performance suggests that these C@MoS₂ composites with unique flower-like morphology could be a promising candidate as an anode material for lithium-ion batteries.

1. Introduction

Battery energy storage technologies and/or materials are required to meet the increasing demand of constant power supply,[1–3] while addressing the environmental concerns. Lithium-ion batteries (LIBs) with high energy density, high voltage, and long lifespan have now become one of the predominant energy storage technologies and power sources for portable electronics, electric vehicles (EVs), and hybrid electric vehicles (HEVs). To meet the demands for use in EVs and HEVs, substantial efforts have been devoted to developing new and better electrode materials and new structures with high energy and power density that also offer better cyclic stability.[4–6] During the past several decades, extensive studies have been focused on tailoring materials towards the nanoscale.[7] Large specific surface area and confined material dimension, which are the characteristics of the nanoscaled materials, impart a high

lithium-ion intercalation capacity, shortened diffusion lengths and large contact area for enhanced kinetics.[8–12] Graphite has been commonly used as an anode material, but it has a low theoretical specific capacity of 372 mA h g⁻¹ due to the limit of thermodynamic equilibrium saturation composition of LiC₆,[13] and leads to difficulties in fulfilling the increasing demand for high performance lithium-ion batteries. In this regards, alternative anode materials such as transition metal oxide,[14–18] and transition metal sulfide,[19] corresponding to a much higher capacity, are studied.

Among a variety of possible anodic materials, molybdenum disulfide has gradually drawn attention for becoming a potential candidate for next-generation LIBs, owing to its high theoretical specific capacity (∼670 mA h g⁻¹) and improved cyclic stability. MoS₂, consisting of molybdenum atoms sandwiched between two layers of closely packed sulfur atoms, is an inorganic graphene analog layered structure where the two-dimensional molecular layers are weakly linked by van der Waals interactions,[20,21] The weak van der Waals forces allow a fast diffusion path for movement of lithium-ion without a significant increase in volume expansion.[22,23] Because of this special S–Mo–S layered structure, it is favorable for lithium-ion insertion/extraction during the discharge–charge process.[24,25] Theoretically, MoS₂ can store 4 moles of lithium-ion based on a redox conversion reaction, where the MoS₂ is reduced to Mo nanocrystals dispersed in a Li₂S matrix upon lithiation, which are then reversibly restored to corresponding disulfide after delithiation, leading to higher reversible theoretical capacities than

[a] State Key Laboratory of Advanced Technology for Materials Synthesis and Processing, School of Materials Science and Engineering, Wuhan University of Technology, Wuhan, 430070, P. R. China. E-mail: chenw@whut.edu.cn; Fax: +86-27-87760129; Tel: +86-27-87651107

[b] Department of Materials Science and Engineering, University of Washington, Seattle, Washington, 98195, USA. E-mail: gzcao@u.washington.edu; Fax: +1-206-543-3100; Tel: +1-206-616-9084

[c] Department of Mechanical Engineering Technology, Purdue University, West Lafayette, Indiana, 47906, USA

† Electronic supplementary information (ESI) available. See DOI: 10.1039/c4ta01247j

that of commercial graphite as anode material.[26] In addition, MoS_2 has also attracted considerable attention as a safe anode material due to its relatively higher lithium-ion insertion voltage than that of commercial graphite anode.[27] In spite of these advantage, the practical use of bulk MoS_2 materials is seriously hindered by the poor capacity retention over extended charge–discharge cycling. This problem mainly originates from the intrinsic poor electrical/ionic conductivity and severe destruction upon repetitive lithium insertion during alloying/dealloying. The poor conductivity and structural pulverization leading to a rapid decay in capacity and poor high-rate properties, thus limit the potential application. Therefore, it remains a great challenge to develop new strategies that improve the poor cycling performance and decreased capacities of bulk MoS_2 electrodes.

To alleviate these issues, one effective measure to attain the objective is to optimize the MoS_2 to well-designated nanostructures with a larger surface area, shorter diffusion path, and controllable morphology.[28–30] To date, various MoS_2 nanomaterials, including nanosheets, nanoparticles, hybrids, and mesoporous structures of MoS_2 have been widely studied due to their higher capacity and improved cycling performance compared with MoS_2 bulk.[31–34] For example, Ding et al. reported the fabrication of MoS_2 microspheres composed of few-layered nanosheets, which showed a high discharge capacity of 672 mA h g^{-1} at a current density of 100 mA g^{-1} after 50 cycles.[35] Similarly, layered MoS_2/graphene composites obtained by a L-cysteine-assisted solution-phase method exhibited the highest specific capacity of ~1100 mA h g^{-1} at a current density of 100 mA g^{-1} and no capacity fading after 100 cycles.[36] Yang et al. synthesized MoS_2/polyaniline nanowires structure, which delivered a capacity of about of 952.6 mA h g^{-1} at a current density of 100 mA g^{-1} with a good capacity retention after 50 cycles. Another strategy to solve the capacity fading problem is by making use of the fabrication conductive hybrids based on MoS_2 and carbonaceous matrix materials. For example, Zhou et al. formed MoS_2@CMK-3 nanocomposite as an anode material for lithium-ion batteries, and it exhibited an improved cycling performance of 602 mA h g^{-1} at 250 mA g^{-1} after 100 cycles and had an excellent rate capability of 564 mA h g^{-1} at 2000 mA g^{-1}.[37] The growth of MoS_2 nanosheets on carbon nanotubes can exhibit high capacity and excellent cycling performance which remains at 823 mA h g^{-1} even after 30 cycles that when cycled at a current density of 100 mA g^{-1}.[38] Thus, the capacity and cycling performance of MoS_2-based LIBs were improved greatly by the above approach. However, owing to the van der Waals interactions, the exfoliated MoS_2 layers tend to aggregate or restack during repetitive cycling, which would lead to the capacity fading and poor stability. Inspired by the research above, if a flower-like MoS_2 can be synthesized by a facile route, which will provide a great technological promise for a variety of sustainable applications.[39] And if the flower-like MoS_2 are uniformly coated by carbonaceous matrix materials, their aggregation can be effectively suppressed, which results in the improved electrochemical properties. Therefore, it is helpful to combine the two strategies, which is about a facile and one-pot synthesis of carbon coated MoS_2 composite with

enhanced high capability. Hence, a robust composite structure and optimum-designed hybrid can be obtained, which may be a promising candidate as an anode material for the LIBs with high-performance.

Herein, we report a simple chemical process for the fabrication of carbon coated MoS_2 nanosheets composites (denoted as C@MoS_2) by means of hydrothermal growth followed with a pyrolysis. This method is environmentally friendly, does not require toxic reagents and solvents. In addition, it is readily to the acquisition of the raw materials, and is scalable to an industrial level or business application. The flower-like C@MoS_2 composites is successfully fabricated, which is composed of ultrathin nanosheets. The effects of the carbon on the nanostructures and electrochemical performances of the composites as lithium-ion battery anodes are systematically investigated. It is found that the right amount of carbon not only improves the electrical conductivity of the electrode, but also effectively ensures the structural stability of the materials during the lithium-ion insertion/desertion process. When evaluated as an anode material for lithium-ion batteries, the as-synthesized optimal-designed C@MoS_2 composites exhibit enhanced electrochemical properties with relatively good cycling stability and high reversible capacity in the high current rate.

2. Experimental section

2.1 Materials synthesis

C@MoS_2 composites were synthesized via a facile one-pot hydrothermal method followed by thermal treatment. In a typical reaction, 0.14 g of MoO_3 (Alfa Aesar), 0.18 g of D-glucose (Sigma-Aldrich), 0.16 g of thiacetamide (Sigma-Aldrich) and 1.4 g of urea (Sigma-Aldrich) were combined with 10 mL of ethanol (Sigma-Aldrich) and dissolved in distilled water. After being stirred for several minutes, the solution was then transferred into a polytetrafluoroethylene (PTFE)-lined, 50 mL capacity stainless steel autoclave and kept at 200 °C for 24 h. After the autoclave was cooled down, the precipitate was isolated and washed several times by centrifugation with deionized water, followed by drying at 60 °C overnight. The composites were annealed in a conventional tube furnace at 800 °C for 2 h under nitrogen flow. The C@MoS_2 composites synthesized utilizing this 1 : 1 molar ratio of D-glucose to MoO_3 was designated as C@MoS_2 (1 : 1). Correspondingly, C@MoS_2 composites with 2 : 1 (carbon was prepared by 0.36 g of D-glucose) and 4 : 1 (carbon was prepared by 0.72 g of D-glucose) molar ratios of Mo to D-glucose were obtained using the same synthesis route as well and were designated as C@MoS_2 (2 : 1) and C@MoS_2 (4 : 1), respectively.

2.2 Materials characterization

The crystal structure of the obtained samples was characterized by means of X-ray diffraction (XRD, D8 Bruker X-ray diffractometer with Cu-Kα radiation ($\lambda = 1.5418$ Å)). The surface morphology and composition of the sample was examined using scanning electron microscopy (SEM, JEOL JSM-7000F)

This journal is © The Royal Society of Chemistry 2014

J. Mater. Chem. A, 2014, 2, 7862–7872 | 7863

and energy dispersive X-ray spectroscopy. Transmission electron microscopy (TEM) was carried out using an FEI, Tecnai G2 F20 transmission electron microscope operating at 200 kV accelerating voltage. The compositional analysis and elemental mapping on the as-prepared sample was performed with an energy-dispersive X-ray spectroscopy (EDX) system, an accessory of SEM. The Brunauer–Emmett–Teller (BET) specific surface areas and pore size distributions were measured with QuantaChrome NOVA 4200e analyzer. Thermogravimetric analysis (TGA) was performed on a TG instrument (NET ZSCH STA 409C). X-ray photoelectron spectroscopy (XPS) analysis was performed using a VG Multilab 2000 with Al Kα as the X-ray source.

Fig. 1 XRD patterns of (a) MoS_2, (b) C@MoS_2 (1 : 1), (c) C@MoS_2 (2 : 1) and (d) C@MoS_2 (4 : 1) composites prepared by hydrothermal route and annealing in N_2 at 800 °C for 2 h.

2.3 Electrochemical measurement

To evaluate the electrochemical performance, coin-type half-cells were assembled using the as-prepared samples as anode materials for lithium-ion batteries. The as-prepared active material was prepared by mixing the as-synthesized C@MoS_2 composites, Super P conductive carbon (TIMCAL Graphite & Carbon), and poly(vinylidene fluoride) (PVDF, Sigma-Aldrich) binder dispersed in a N-methyl-2-pyrrolidone (NMP, Alfa Aesar) solution at a weight ratio of 80 : 10 : 10, respectively. The as-prepared active material slurry was uniformly spread onto Cu foil and dried in a vacuum oven at 80 °C overnight prior to coin-cell assembly. The mass of the active material is approximately 1 mg, depending on the thickness of film formed on Cu current collector. The electrochemical experiments were performed using CR2016-type coin cells, which were assembled in an argon-filled dry glovebox (Innovative Technology, IL-2GB) with C@MoS_2 composites as the working electrode, pure lithium foil as the counter and reference electrodes, polypropylene membrane film as the separator, and 1 M $LiPF_6$ in ethylene carbon (EC)–dimethyl carbonate (DMC) as electrolyte. Galvanostatic discharge and charge measurements were performed under different current densities in the voltage range between 0.01 V and 3.0 V at room temperature. Cyclic voltammetry (CV) was conducted on an electrochemical analyzer (CH Instruments, model 605C) in the voltage range of 0.01–3.0 V ($vs.$ Li/Li$^+$) at a scan rate of 0.2 mV s^{-1}. Alternating current (AC) impedance was recorded by applying the Solartron 1287A in conjunction with a Solartron 1260FRA/impedance analyzer with amplitude of 5.0 mV in the frequency range from 100 kHz to 0.01 Hz. The half-cells were tested at various current rates based on the weight of the active material alone.

3. Results and discussion

The crystalline structure and crystallinity of the as-prepared material are confirmed by X-ray diffraction (XRD), the results of which are displayed in Fig. 1. All the diffraction peaks of samples can be indexed to the hexagonal MoS_2 phase with lattice parameters $a = 3.16$ Å, $b = 3.16$ Å, $c = 12.30$ Å, and $\beta = 90.00°$, which are in good agreement with the literature values (JCPDS: 00-037-1492). No diffraction peaks from impurities or parasitic phases are observed. As shown in Fig. 1a–d, the
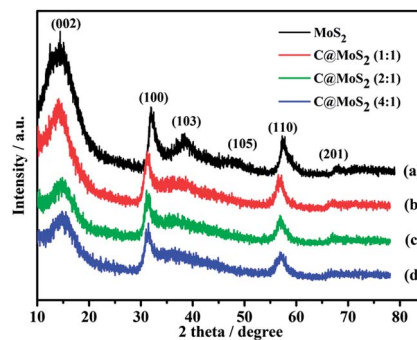
crystallinity and peak positions of MoS_2 are retained with increasing amounts of carbon. Additionally, the diffraction peaks of carbon could not be observed. This result may be attributed to carbon derived from D-glucose being amorphous. However, Fig. 1b–d confirm that the intensity of all the diffraction peaks gradually decreased as the amount of carbon in the composites increased. Furthermore, the MoS_2 peaks had weaker intensities than that of the bare MoS_2 specimen, which suggests that continuous crystal growth has been effectively inhibited by the incorporation of carbon coating on the flower-like MoS_2 nanosheets.[40] Interestingly, the gradual narrowing of the (002) plane peak may suggest that the number of (002) planes in MoS_2 decreased after the inclusion of carbon, which resulted in ultrathin MoS_2 nanosheets; in other words, these XRD findings indicate that the composites contain fewer stacking layers of MoS_2. In particular, the lattice parameters of the C@MoS_2 (2 : 1) (Fig. 1c) calculated from the corresponding XRD pattern are $a = 3.12$ Å and $c = 12.54$ Å at $2\theta = 14.12°$. These findings differ from the excepted value according to literature calculations, the discrepancy of which is attributed to internal stress from the curved and folded layers. In other words, increasing the layer spacing is favorable towards providing broadened channels for the lithium-ion diffusion during the insertion/desertion process.[41] The interlayer spacing of the phase is calculated to be 6.3 Å from the (002) diffraction peak. According to the Scherrer equation, peak analysis of the (002) XRD peak indicates that the average crystallite size is approximately 21 Å, which equates to approximately 3 layers of MoS_2; these findings are in accordance with the HRTEM results that the C@MoS_2 composites are composed of nanosheets.

Fig. 2 presents a general view of the morphologies of MoS_2, C@MoS_2 (1 : 1), C@MoS_2 (2 : 1), and C@MoS_2 (4 : 1) composites prepared by hydrothermal route followed by a heat treatment. From the scanning electron microscopy (SEM) image (Fig. 2a), it is found that rounded flake type morphology of MoS_2 is obtained, which has dispersed to form a disordered stacking sequence. When the carbon coating is present after the annealing process, the synthesized C@MoS_2 composites display a nanoflower morphology consisting of nanosheets, as shown in Fig. 2b–d. Interestingly, the sheet-like subunits are interconnected by sharing one edge to form a three-dimensional
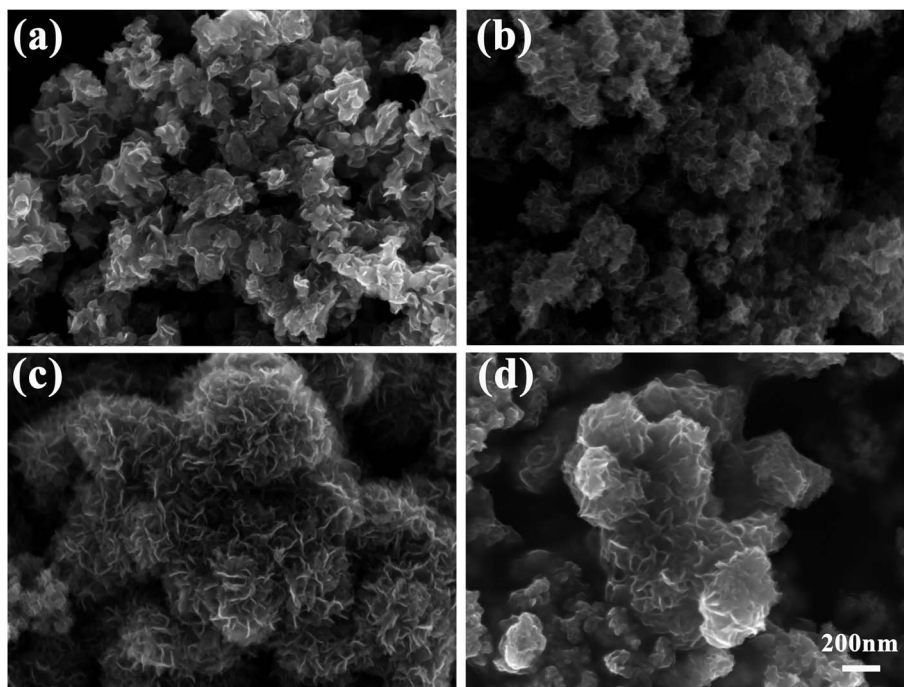
7864 | *J. Mater. Chem. A*, 2014, **2**, 7862–7872

This journal is © The Royal Society of Chemistry 2014

Fig. 2 SEM images of (a) MoS_2, (b) C@MoS_2 (1 : 1), (c) C@MoS_2 (2 : 1) and (d) C@MoS_2 (4 : 1) composites prepared by hydrothermal route and annealing in N_2 at 800 °C for 2 h. (All the images have the same scale.)

nanostructure when carbon was introduced into the system. In particular, the flaky C@MoS_2 (2 : 1) composites, with wall thickness in the range of 5–10 nm, are attached to each other by van der Waals interaction and finally self-assembled into the three-dimensional nanostructures (Fig. 2c). These ultrathin nanosheets create loose porous nanostructures with ample open space and electroactive surface sites for lithium-ion diffusion and insertion/desertion reaction. Fig. 2d shows that the C@MoS_2 (4 : 1) composites still retain the nanoflower morphology with ambiguous interface, however, the excessive carbon coating on MoS_2 may lead to obvious agglomeration.

To provide further insight into the morphology and structure of the resulting C@MoS_2 (2 : 1) composites, the flower-like microstructure is also viewed under transmission electron microscopy (TEM). Fig. 3a depicts a nanoflower microstructure which exhibits rippled sheets morphology due to its ultrathin features. By closer observation shown in Fig. 3b, the nanosheets constituents can be clearly seen with bending, curling, and overlapping flakes and they are 5–10 nm in thickness. The crumpling nanosheet morphologies interconnect with each other *via* self-assembly of the carbon coating on the surface. The morphology and size of the sample obtained from TEM matches well with those observed from the SEM images. A TEM image (ESI, Fig. S1†) reveals that a thin carbon overcoat (approximately 0.86 nm thick) has formed from the carbonization of polysaccharide that coated every crystallite to form a C@MoS_2 core–shell structure. Fig. 3c shows a high-resolution TEM (HRTEM) image taken from the edge of nanosheets, which provides more detailed structural information. It can be clearly noted that the typical layered MoS_2 is composed of fewer layers (3–5) with an overlaying amorphous carbon coating. The observed lattice

spacing of 6.3 Å corresponds to the inter-plane spacing of (002) of hexagonal MoS_2, slightly larger than the reported data (6.15 Å), and is consistent with the results obtained from the XRD pattern. HRTEM of the layered MoS_2 and the corresponding FFT pattern (the inset in Fig. 3d) reveal that the C@MoS_2 composites are weakly crystalline. It is clearly that three nanoparticles, marked by the dotted cycles can be seen in this image. Lattice fringes with spacing of 0.26 and 0.22 nm are in good agreement with the *d*-spacing of the (100) and (103) planes of MoS_2, respectively. The carbon content of the prepared C@MoS_2 (2 : 1) composite is measured using thermogravimetric analysis and comprised ~23 wt% of the specimen (ESI, Fig. S2†). N_2 adsorption/desorption measurement shows that the C@MoS_2 (2 : 1) composites possess a Brunauer–Emmett–Teller (BET) specific surface area of 31 m^2 g^{-1}, which is higher than the calculated surface area (ESI, Fig. S3†). Additionally the pore distribution is mainly centered at 4 nm, which is in the mesoporous range. These results also corroborate that the curved and bending MoS_2 nanoflowers are composed of several stacked sheet subunits. Such flower-like structures are attractive for energy storage applications due to their enlarged specific surface areas and the ultrathin thickness of the nanosheet subunits. Specifically, it is known that the three-dimensional flower-like structures are beneficial in facilitating the shorter lithium-ion diffusion channels. Moreover, the appropriate carbon coating can form an interconnected conductive network which will also greatly increase the electrical conductivity and the mass transport of the electrolyte within the electrodes for fast redox reactions during the charge–discharge process. However more importantly, the ultrathin nanosheet
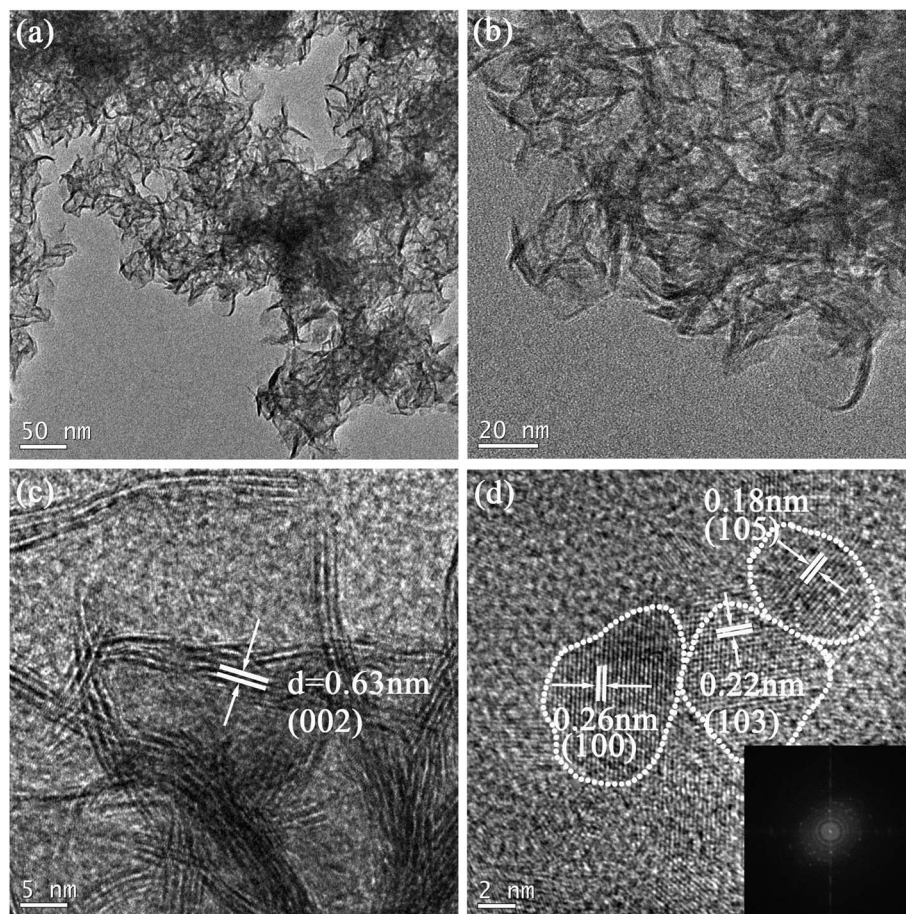
Fig. 3 Microstructure of C@MoS$_2$ (2 : 1) composites: (a) SEM image, (b) TEM image, (c) HRTEM image, and (d) HRTEM of layered MoS$_2$ and the inset of (d) shows the corresponding FFT pattern.

structures provide enlarged electrode–electrolyte contact area, and thus further enhance the electrochemical performance.

In order to analyze the composition of the samples, EDX of the layered C@MoS$_2$ composites was performed; the element compositions of C@MoS$_2$ composites with different carbon contents are displayed in Table 1. The EDX measurements confirm the co-existence of Mo, S, C, and O elements (wt% corresponding to the mean weight ratio in different parts of the composite) with no detectable impurities. It is evident that carbon emanates from the reduction of glucose, while a small amount of oxygen is attributed from the incomplete decomposition of glucose and partially oxidized Mo. By calculating the

element contents of the different C@MoS$_2$ composites, the atomic ratio of Mo and S turns out to be in the range of 1.75 to 1.83, considering the fact that EDS has a ~10% error. In addition, these values also show that the atomic ratio of C to Mo are closer to the theoretical values of the molar ration of $n_{glucose/Mo}$ (1 : 1, 2 : 1, 4 : 1) in the C@MoS$_2$ composites. From the EDX analysis, it has been proven that the addition of glucose is crucial to the formation of the C@MoS$_2$ nanoflowers.

XPS analysis was carried out in the region of 0–1100 eV on a VG Multilab 2000 to elucidate the chemical composition of C@MoS$_2$ (2 : 1) composites. Before the measurement, this instrument has a monochromatized Al Kα X-ray source and a low energy electron flood gun for charge neutralization. Fig. 4a shows that the sample contains the Mo, S, C and O elements. The peaks of Mo (Mo 3d$_{5/2}$, 3d$_{3/2}$) and S (S 2p) in the survey spectrum can be assigned to the characteristic of MoS$_2$. Fig. 4b shows the high-resolution spectrum of Mo 3d. Two peaks are located at 229.2 and 232.4 eV, respectively, which are attributed to the doublet Mo 3d$_{5/2}$ and Mo 3d$_{3/2}$, characteristic of Mo^{4+} in MoS$_2$. And a small S 2s peak is located at 226.6 eV, which is a slightly lower binding energy than the Mo 3d$_{5/2}$ peak. Fig. 4c shows the binding energies of S 2p peaks, corresponding to the S 2p$_{1/2}$ and S 2p$_{3/2}$ orbital of divalent sulfide ions (S^{2-}), which

Table 1 Element composition of C@MoS$_2$ composites after annealing in N$_2$ at 800 °C for 2 h with different carbon contents

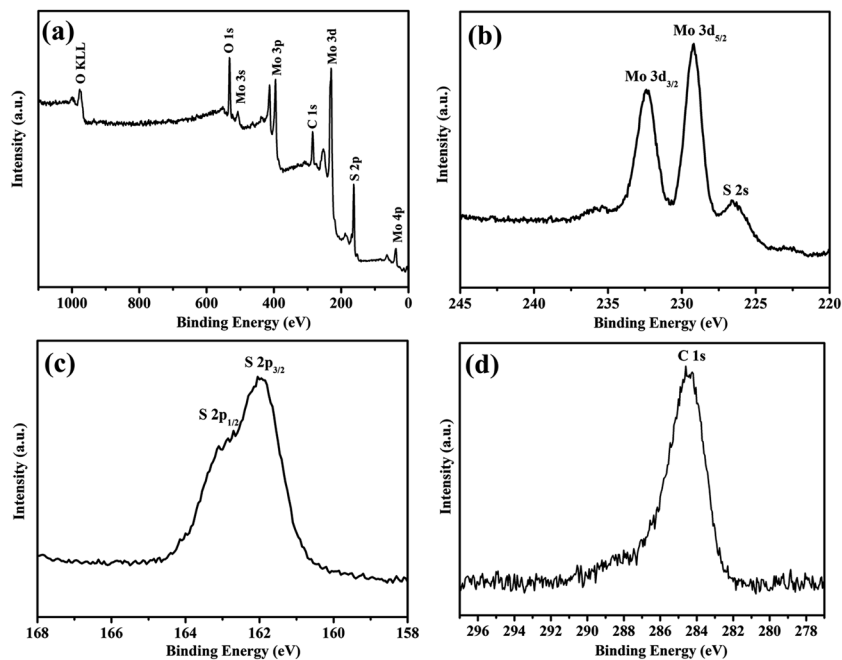| Nanocomposite	Element (wt%)			
	C	O	S	Mo
MoS$_2$	0	0	35.97	64.03
C@MoS$_2$ (1 : 1)	30.54	4.52	23.97	40.97
C@MoS$_2$ (2 : 1)	39.21	3.08	21.32	36.38
C@MoS$_2$ (4 : 1)	60.35	3.61	13.56	22.49

Fig. 4 (a) Wide survey XPS spectrum of C@MoS$_2$ (2 : 1) composites. (b) Mo 3d spectrum. (c) S 2p spectrum. (d) C 1s spectrum.

are observed at 163.1 and 162.2 eV. These surveys are in good agreement with the values reported in the literature for MoS$_2$ crystal.[42–44] In Fig. 4d, the C 1s XPS spectrum consists of five types of carbon species, with the strong peak at 284.6 eV assigned to the C–C bonds in the carbon frameworks, while the weak ones C–OH at 285.9 eV, C–O–C at 287.5 eV, C=O at 288.3 eV and C(O)–C at 289.2 eV. The existence of those four small peaks suggests the presence of some residual groups from the insufficient reduction of glucose.[15]

There are some possible proposed formation mechanisms as follows (shown in Scheme 1): (i) MoO$_3$ is firstly dissolved in distilled water, which acts as the precursor and self-template in the following hydrothermal process. When in the hydrothermal surroundings, MoO$_2$ seed crystals are formed in the solution *via* the reduction of ethanol. This step has been documented in the literature.[45–47] (ii) Under the synthesis conditions employed by thioacetamide in the present research, MoS$_2$ is then formed into the nanoflower structures with ultrathin sheets, where van der Waals interaction is the major binding between the stacked sheets. It can be concluded that the bond breaking along the (002) direction consumes less energy.[48] It is obvious that the cleavage along the axial direction of the nanosheets is much
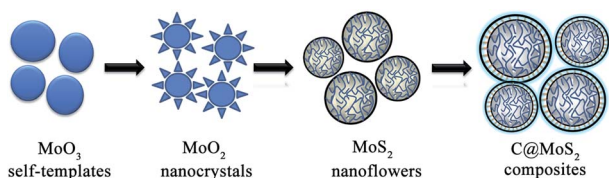
easier to carry out and afterwards split into the ultrathin sheets. (iii) The glucose coats the nanoflower structures and serves as a carbon source for the *in situ* formation of the carbon coating on the MoS$_2$ nanosheets in a reducing atmosphere. Furthermore, after the annealing process, a thin carbon layer is simultaneously generated on the surface of the nanosheets from carbonization of the polysaccharide; as a result, the sheet-like morphology can be retained. The appropriate amount of glucose serves as a capping agent to prevent the overgrowth of the primary MoS$_2$ crystals, as well as over-agglomeration of the assembled MoS$_2$ nanoflowers as shown in Fig. 2c and 3a. In comparison, the MoS$_2$ sample prepared without glucose was composed of disordered platelet-like structures with no densely stacked sheet-like subunits (Fig. 2a). Therefore, glucose not only serves as the carbon source, but also restrains the overgrowth of the MoS$_2$ crystals.

To understand the lithium-ion storage properties of the C@MoS$_2$ composites, cyclic voltammetry (CV), galvanostatic charge–discharge measurements and electrochemical impedance analysis have been performed. Fig. 5 depicts the first, second, and fifth CV curves of the pure MoS$_2$ and C@MoS$_2$ (2 : 1) composites collected at a scan rate of 0.2 mV s^{-1} in the voltage range of 0.01–3.0 V, parameters which are consistent with the literature.[49–51] As shown in the first cathodic sweep of Fig. 5b, an ambiguous peak at approximately 0.9 V corresponds to the phase transition from trigonal prismatic to octahedral coordination which is driven by a lowering of the electronic energy for the octahedral structure when electrons are donated from the lithium-ion to MoS$_2$. In other words, the peak results from the intercalation of lithium-ion on different defect sites of MoS$_2$ to form Li$_x$MoS$_2$ according to eqn (1). The pronounced peak located at 0.5 V is likely to be related to the following
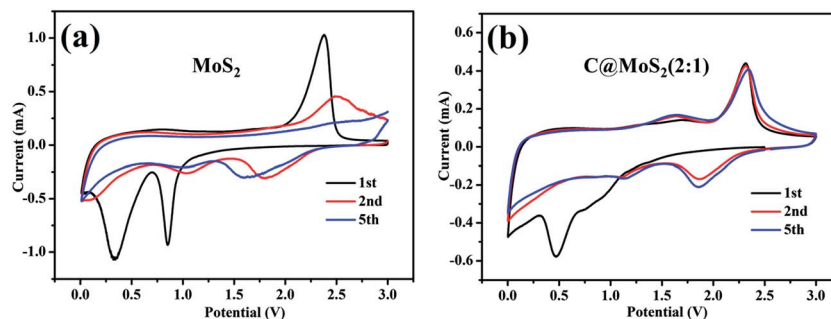

Scheme 1 Schematic depicting the formation of C@MoS$_2$ composites.

Fig. 5 CV curves of (a) pure MoS_2, (b) $C@MoS_2$ (2 : 1) measured in the voltage range of 0.01–3.0 V with a scan rate of 0.2 mV s^{-1}.

reactions according to the eqn (2), which first entails the *in situ* decomposition of MoS_2 into Mo nanoparticles embedded into a Li_2S matrix and then the formation of a gel-like polymeric layer resulting from electrochemically driven electrolyte degradation.[52] In the reverse anodic scan, a very small oxidation peak at 1.7 V is found, corresponding to the partial oxidation of Mo. A more pronounced peak at 2.3 V could be attributed to the oxidation of Li_2S into S according to eqn (3). It is also noted that the slight shifts in the reduction peak potentials or changes in the reduction peak shape could be caused by the overlap of electrochemical lithium-ion storage in both MoS_2 and carbon compared to the bare MoS_2.[53,54] In the following cycles, the reduction peaks at 0.5 V and 0.9 V disappear and two new peaks at 1.2 V and 1.8 V are observed, which indicates the multistep conversion from S with lithium-ion to finally the formation of Li_2S. The CV profiles are very stable and remain steady after the first cycle, indicating the materials have a high reversibility and good stability for the insertion and desertion of lithium-ion. For the bare MoS_2 electrode, two redox peaks located at 0.3/0.85 V and 2.3 V in the first cycle correspond to the conversion reaction process: $MoS_2 + 4Li^+ + 4e^- \rightarrow Mo + 2Li_2S$, which agrees well with the previous lithiation and delithiation profiles of $C@MoS_2$ composites. In the subsequent cycles, however, the anodic peaks intensity decreased sharply, suggesting an irreversible conversion reaction during the lithium-ion insertion/extraction process. It is also noteworthy to mention that the shape of the peaks for the $C@MoS_2$ composites is sharper and more intense, and the gap between redox peaks is smaller than that for the bare MoS_2, demonstrating that the former had a lower overall resistance and greater efficiency of the redox reaction.[55]
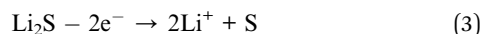
$$MoS_2 + xLi^+ + xe^- \rightarrow Li_xMoS_2 \qquad (1)$$

$$Li_xMoS_2 \rightarrow xLi_2S + Mo \qquad (2)$$

$$Li_2S - 2e^- \rightarrow 2Li^+ + S \qquad (3)$$

Fig. 6 displays the charge–discharge profiles of the bare MoS_2 and $C@MoS_2$ composites with various carbon contents for the initial three cycles in the voltage range of 0.01 to 3.0 V at a current density of 100 mA g^{-1}. Specifically, as shown in Fig. 6a, there are two plateaus located at approximately 1.2 and 0.7 V on the discharge curves, which are in qualitative agreement with

the CV measurements of the bare MoS_2. These results suggest the lithium-ion intercalate to form Li_xMoS_2, whereupon the conversion reaction occurs by two steps. In the second and third discharge curves, two potential plateaus at 2.0 and 1.2 V are observed and the potential plateau at 0.7 V in the first discharge disappears. Interestingly, the discharge potential plateau of the bare MoS_2 experiences a conspicuous profile whereas the potential plateau of the $C@MoS_2$ composites appear to be ambiguous with the increasing carbon contents (Fig. 6b–d). This phenomenon may be existence consequence of amorphous carbon in the composite leading to poor crystallinity, which corroborates the findings from the FFT pattern (inset of Fig. 3d). Furthermore, an overlapping electrochemical lithium-ion storage mechanism caused by both MoS_2 and carbon may be taken into consideration. During the charge process, one plateau at 2.3 V is observed for all the samples with various carbon contents, and corresponds to the reversible extraction of lithium-ions. The initial discharge capacities of the MoS_2, $C@MoS_2$ (1 : 1), $C@MoS_2$ (2 : 1), and $C@MoS_2$ (4 : 1) are found to be 885, 1197, 1419, and 944 mA h g^{-1} while the charge capacities are 723, 879, 988, and 719 mA h g^{-1}, respectively. The coulombic efficiency of the MoS_2, $C@MoS_2$ (1 : 1), $C@MoS_2$ (2 : 1) and $C@MoS_2$ (4 : 1) are 81.7%, 73.4%, 69.7%, and 76.2% which experience serious decay. The irreversible capacity loss in the first cycle is inevitable for the majority of transition metal sulfides, and according to previous reports[38,51] is ascribed to the formation of the solid electrolyte interphase and electrolyte degradation. Among these samples, $C@MoS_2$ (2 : 1) composites have the highest charge–discharge capacities. Moreover, it can retain good stability after three cycles. As shown in Fig. 7, the graph directly compares the discharge capacity of the bare MoS_2, $C@MoS_2$ (1 : 1), $C@MoS_2$ (2 : 1), and $C@MoS_2$ (4 : 1) samples during the 5th cycle. All the samples in the 5th cycle possess a good discharge capacity, but the capacity of the $C@MoS_2$ (2 : 1) sample (~1140 mA h g^{-1}) is generally higher than those of the other samples. These results indicate that the optimum design of the $C@MoS_2$ composites occurs at a precursor ratio of 2 : 1 and leads to a uniform thin carbon coating that enables enhanced electrical conductivity which ultimately benefits the lithium-ion storage capacity. Therefore, the greatly enhanced lithium-ion storage properties of the $C@MoS_2$ (2 : 1) composites in comparison to other samples may be attributed to its interpenetrating conductive carbon
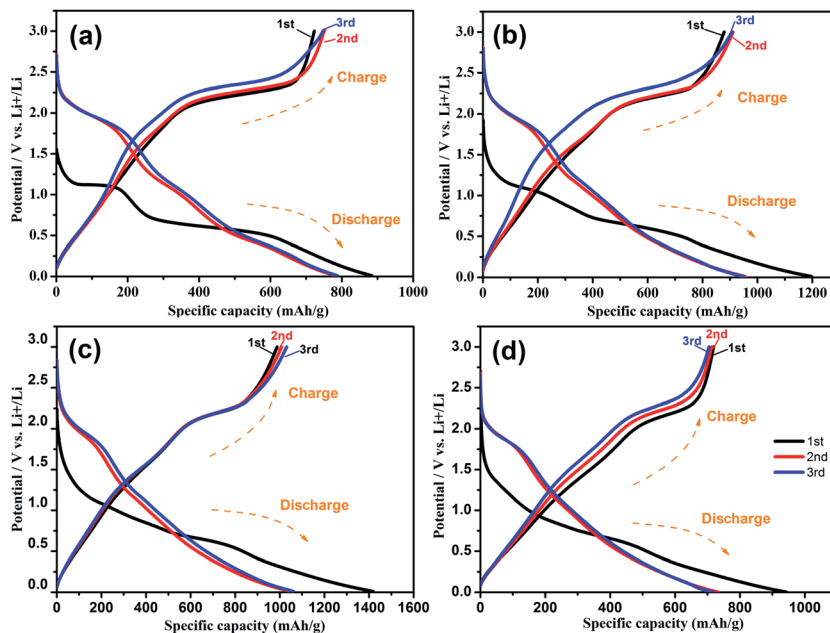
Fig. 6 First three discharge and charge curves of the samples after annealing in N_2 at 800 °C for 2 h at a current density of 100 mA g^{-1} in a half-cell composed of C@MoS$_2$ and Li: (a) MoS$_2$, (b) C@MoS$_2$ (1 : 1), (c) C@MoS$_2$ (2 : 1) and (d) C@MoS$_2$ (4 : 1).
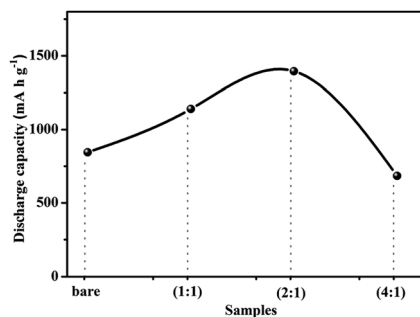

Fig. 7 Comparison of the 5th discharge capacity of the (a) bare MoS$_2$, (b) C@MoS$_2$ (1 : 1), (c) C@MoS$_2$ (2 : 1) and (d) C@MoS$_2$ (4 : 1) composites at a current density of 100 mA g^{-1}.

network and monodisperse nanosheet structure, resulting in better ionic and electronic conduction throughout the electrode.

The cyclic stability and coulombic efficiency of the bare MoS$_2$ and C@MoS$_2$ (2 : 1) composites at a current density of 100 mA g^{-1} are presented in Fig. 8. It is apparent that the electrochemical performance of the C@MoS$_2$ (2 : 1) composites is superior to that of the bare MoS$_2$ electrode which undergoes a severe capacity drop upon cycling. The reversible capacity of the bare MoS$_2$ dramatically decreases to 110 mA h g^{-1} after 50 cycles. In contrast, the C@MoS$_2$ (2 : 1) composites still retain a reversible capacity of 837 mA h g^{-1} after 50 cycles, reaching 80% of the original capacity which attests to the good stability. The enhanced capacity is attributed to the formation of the gel-like polymeric layer and possibly interfacial lithium-ion storage as well as electrochemical activation of the hybrid structure during the cycling process. Such behavior has been previously reported

as well.[52,56] The residual oxygen groups from the insufficient reduction of glucose may also make contribution to the enhanced capacity. The residual oxygen groups would increase active pathway for lithium-ions storage, which is facile to the interfacial electrochemical reaction. Interestingly, when a various amount of glucose is added during the hydrothermal process, not only does the initial capacity double from that of the bare MoS$_2$ but the capacity retention is significantly improved, as shown in Fig. 8. According to the weight proportion of MoS$_2$ in the C@MoS$_2$ (1 : 2) composites (57.70 wt% MoS$_2$ in Table 1) and the capacity of the amorphous carbon (180 mA h g^{-1}), it is calculated that the specific capacity of MoS$_2$ in the C@MoS$_2$ (1 : 2) composites is up to 1610 mA h g^{-1}, which are much higher than that of the exfoliated MoS$_2$ (1131 mA h g^{-1}) reported by Lemmon et al.[57] It isn't considered that such a high capacity is attributed to only the flower-like MoS$_2$ nanosheets. Therefore, the high specific capacity of the
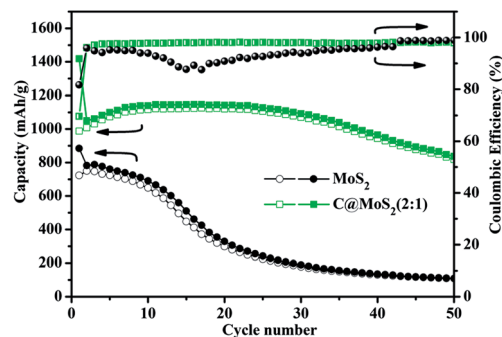

Fig. 8 Cycling performance and their columbic efficiencies of bare MoS$_2$ and C@MoS$_2$ (2 : 1) composites electrodes at a current density of 100 mA g^{-1}.

This journal is © The Royal Society of Chemistry 2014

J. Mater. Chem. A, 2014, 2, 7862–7872 | 7869

C@MoS$_2$ (1 : 2) composites is ascribed not only to the robust composite structure, but also to the incorporation of the carbon and the unique nanocomposites architecture of expanded layers distances of MoS$_2$ nanosheets. In addition, the coulombic efficiency of the C@MoS$_2$ (2 : 1) composites rises rapidly from 70% in the 1st cycle to 96% in the 2nd, and remains at approximately 98% in the following cycles. To the contrary, the efficiency of the bare MoS$_2$ fluctuates considerably, and stays at a low level compared to the C@MoS$_2$ (2 : 1) composites. It is thus evident that the C@MoS$_2$ (2 : 1) composites exhibit a much improved charge–discharge reversibility compared to the bare MoS$_2$. This enhanced charge–discharge reversibility and superior cycling stability of the C@MoS$_2$ (2 : 1) composites can be attributed to the unique flower-like morphology composed of the ultrathin MoS$_2$ nanosheets and carbon coating nanostructure, featuring a large contact area and interconnected conductive network. For one thing, the large surface area supported by the ultrathin MoS$_2$ nanosheets endows the composite with high specific capacity due to the enhanced interfacial transfer of electrons and the reduction of the effective current density which relieves any damage the active material experiences. Additionally, the flexible characteristic of the ultrathin nanosheets consolidates the robust composite structure; the carbon coating does not only improve the electrical conductivity of the electrode, but also inhibits the restack of the flower-like MoS$_2$ nanosheets and stabilizes the electrode structure during the lithium-ion insertion/extraction process.

The rate capability of MoS$_2$, C@MoS$_2$ (1 : 1), C@MoS$_2$ (2 : 1), and C@MoS$_2$ (4 : 1) samples at various charge–discharge rates are compared in Fig. 9. Among these samples, C@MoS$_2$ (2 : 1) composites show a higher capacity at each current rate. With the benefits of its unique morphology and structure, the C@MoS$_2$ (2 : 1) sample exhibits excellent cycling response to a varying current rate. Specifically, the discharge capacities of the C@MoS$_2$ (2 : 1) sample at the currents densities of 0.1, 0.2, 0.5, 1, 2, 5, and 10 A g^{-1} are 1454, 1359, 1255, 1112, 979, 697, and 672 mA h g^{-1}, respectively, demonstrating the excellent high rate performance for high power lithium-ion battery. Even at a high current density up to 10 A g^{-1}, the C@MoS$_2$ (2 : 1) sample still possesses a better cyclic stability with only 0.22% capacity loss. More importantly, when the current rate is reversed back to 0.1 A g^{-1}, the discharge capacity rebounds to nearly the same
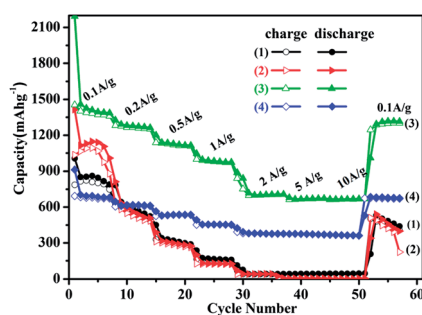
initial capacity ($\sim$1300 mA h g^{-1}). On the contrary, the bare MoS$_2$ electrode and other two MoS$_2$ with different carbon contents deliver much lower capacities at the above mentioned current rates, and fails quickly for the 50th cycle at 10 A g^{-1}. It is obvious that the capacity of bare MoS$_2$ fades rapidly and cannot recover to the initial level even at 0.1 A g^{-1} after high rate cycling. These results show that only with the optimal molar ration of MoS$_2$ to glucose, the composite can exhibit enhanced lithium-ion storage properties, as a promising anodic for high energy density LIBs.

For a better understanding of the electrochemical performance of the C@MoS$_2$ samples compared with the bare MoS$_2$ electrode for lithium-ion energy storage, Nyquist plots of the AC impedance analysis were compiled (Fig. 10). As shown in Fig. 10, the high frequency semicircle could be attributed to resistance R_f of the SEI film, the medium frequency semicircle to the charge transfer resistance R_{ct} of the electrode reaction of the electrode–electrolyte interface. And an inclined line in the low frequency region is descriptive of the lithium-ion diffusion impedance.[58,59] From the Nyquist plots, it is revealed that the C@MoS$_2$ (1 : 1), C@MoS$_2$ (2 : 1), and C@MoS$_2$ (4 : 1) electrodes with different carbon content have a much lower charge transfer resistance (31, 112, 225 Ω) than that of the bare MoS$_2$ electrodes (with the charge transfer resistance more than 400 Ω). These results suggest that the MoS$_2$ with carbon coating possesses lower contact and charge-transfer impedances. In addition, the charge transfer resistance of the C@MoS$_2$ (2 : 1) electrode possesses the smallest value of 31 Ω which is less than 90% of that for the bare MoS$_2$. This smallest value confirms the reduction in contact resistance and charge transfer resistance in lithium-ion insertion/extraction reactions after introducing carbon. According to these results, it can be concluded that the incorporation of carbon not only improves the conductivity of the C@MoS$_2$ composites electrode, but enables the fast transfer of both lithium-ions and electrons during the cycling process, resulting in significant enhancement in the electrochemical properties. Therefore, benefitting from the unique flower-like structure and the presence of carbon coating, the C@MoS$_2$ composites are able to demonstrate excellent reversible capacity, high rate capability and cyclic stability, and show great potential for application as the next generation of anode materials for high energy high power lithium-ion batteries.

Fig. 9 Rate capability of C@MoS$_2$ samples at different current densities: (1) MoS$_2$, (2) C@MoS$_2$ (1 : 1), (3) C@MoS$_2$ (2 : 1) and (4) C@MoS$_2$ (4 : 1).
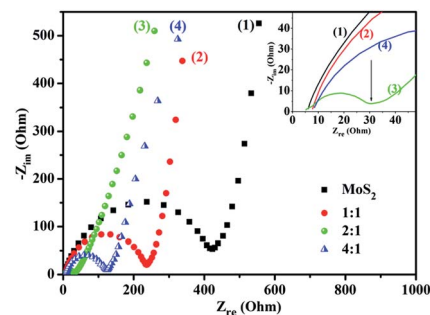

Fig. 10 Nyquist plots of (1) MoS$_2$, (2) C@MoS$_2$ (1 : 1), (3) C@MoS$_2$ (2 : 1) and (4) C@MoS$_2$ (4 : 1) electrodes obtained by applying a sine wave over the frequency range from 100 kHz to 0.01 Hz.

The high reversible capacity and rate capability as well as remarkable cycling performance of the C@MoS$_2$ composites can be ascribed to the MoS$_2$ flower-like structural features and the synergistic effect between the flower-like MoS$_2$ with carbon. Specifically, the three dimensional framework composed of ultrathin nanosheets with large surface areas endows them with shortened lithium-ion diffusion pathway, thus leading to improved electrochemical kinetics of this novel structure. Secondly, XRD and HRTEM demonstrated that the flower-like C@MoS$_2$ composites have expanded interlaminar distances between the MoS$_2$ nanosheets. The increased layer distance between neighboring S–Mo–S layers provides sufficient space for lithium-ion intercalation, thereby facilitating faster lithium-ion diffusion in the MoS$_2$ matrix and enhancing the charge–discharge reversibility. Thirdly, the intrinsic feature of this flower-like MoS$_2$ structure improves the robustness of the electrode structure. Finally, carbon plays a greatly important role in this system. One factor is carbon acting as a binder between the S/Li$_2$S and the molybdenum nanoparticles; for another is that carbon encapsulates both phases providing an electrically conductive path down the current collector and prevents the flower-like MoS$_2$ nanosheets agglomeration during cycling.[60] Moreover, it is helpful to suppress undesired crystal growth and the restack of MoS$_2$ nanosheets. And C@MoS$_2$ composites with the optimal carbon content would facilitate to stabilize the disordered structure of the flower-like MoS$_2$ nanosheets throughout the cycling process to accommodate more lithium-ions intercalation.[57,61,62] Therefore, the synergistic effect between MoS$_2$ nanosheets and carbon is responsible for the high-power performance, excellent rate capability and better cycling stability.

4. Conclusions

A facile hydrothermal method was developed for the synthesis of unique three dimensional flower-like C@MoS$_2$ nanostructures with much improved electrochemical lithium-ions intercalation capacity at a high current rate. In addition, we have experimentally studied and elaborated the effects of carbon on the lithium-ion intercalation properties.

The well-defined nanocomposites were synthesized through the MoO$_3$ acted as the precursor and sacrificial template under the hydrothermal condition and was accompanied with the reduction of glucose and ethanol to form a thin carbon coating on the surface. The as-obtained C@MoS$_2$ composites are composed of ultrathin nanosheets with enlarged interlayer spacing that are self-assembled in an oriented manner in the presence of carbon. More importantly, the optimum designed nanostructure with appropriate carbon contents plays a significant role in morphology and structure of the composites. In particular, the C@MoS$_2$ (2 : 1) composites possess the optimal design formed by ultrathin overlapping flakes with wall thickness of 5–10 nm, which are self-organized into the three-dimensional nanostructures. In such architecture, the overlapped MoS$_2$ nanosheets give rise to high specific surface area and increased layer distance leading to the reduced diffusion path of lithium-ion and rapid electrons transport. Meanwhile,

the flexible and conductive carbon overcoats maintain the structural and electrical integrity of the electrode. As a result of the synergistic effect between the flaky MoS$_2$ and carbon, the electrodes exhibit good lithium-ion storage performance and high coulombic efficiency with superior rate capability. Particularly, C@MoS$_2$ (2 : 1) composites can deliver high reversible specific capacity of 1419 mA h g^{-1} at 0.1 A g^{-1}, and retain 80% of the capacity after 50 cycles. Even at a current density as high as 10 A g^{-1}, the reversible capacity of the C@MoS$_2$ (2 : 1) composites can remain at 672 mA h g^{-1} with almost 100% coulombic efficiency. When the current density returns back to 0.1 A g^{-1} after high rate current, it recovers to the initial value around 1300 mA h g^{-1}. The impedance spectrum also confirms that the faster lithium-ion diffusion is beneficial for the electron penetrating into the electrolyte. Therefore, with rational and optimal design of the C@MoS$_2$ composites, it showed an excellent electrochemical performance which creates a new avenue to develop a high-performance anode material. Our research provides the method that could be readily extended to the synthesis of other layer structured anode materials in order to boost the electrochemical performance of nanomaterials.

Acknowledgements

References

1 M. Dresselhaus and I. Thomas, *Nature*, 2001, **414**, 332–337.
2 J.-M. Tarascon and M. Armand, *Nature*, 2001, **414**, 359–367.
3 M. Armand and J.-M. Tarascon, *Nature*, 2008, **451**, 652–657.
4 J. Liu and X. W. Liu, *Adv. Mater.*, 2012, **24**, 4097–4111.
5 H. Li, Z. Wang, L. Chen and X. Huang, *Adv. Mater.*, 2009, **21**, 4593–4607.
6 K. Evanoff, J. Benson, M. Schauer, I. Kovalenko, D. Lashmore, W. J. Ready and G. Yushin, *ACS Nano*, 2012, **6**, 9837–9845.
7 Y. Shi, J.-Z. Wang, S.-L. Chou, D. Wexler, H.-J. Li, K. Ozawa, H.-K. Liu and Y.-P. Wu, *Nano Lett.*, 2013, **13**, 4715–4720.
8 L. Yang, S. Wang, J. Mao, J. Deng, Q. Gao, Y. Tang and O. G. Schmidt, *Adv. Mater.*, 2012, **25**, 1180–1184.
9 P. G. Bruce, B. Scrosati and J. M. Tarascon, *Angew. Chem., Int. Ed.*, 2008, **47**, 2930–2946.
10 F. Cheng, J. Liang, Z. Tao and J. Chen, *Adv. Mater.*, 2011, **23**, 1695–1715.
11 Y. Wang, H. Li, P. He, E. Hosono and H. Zhou, *Nanoscale*, 2010, **2**, 1294–1305.
12 Y. Shi, J. Gao, H. D. Abruña, H. J. Li, H. K. Liu, D. Wexler, J. Z. Wang and Y. Wu, *Chem. – Eur. J.*, 2014, **20**, 1–6.
13 M. Dresselhaus and G. Dresselhaus, *Adv. Phys.*, 1981, **30**, 139–326.

14 L. Yang, Q. Gao, Y. Zhang, Y. Tang and Y. Wu, *Electrochem. Commun.*, 2008, **10**, 118–122.

15 Y. Sun, X. Hu, W. Luo and Y. Huang, *J. Mater. Chem.*, 2012, **22**, 425–431.

16 Q. Gao, L. Yang, X. Lu, J. Mao, Y. Zhang, Y. Wu and Y. Tang, *J. Mater. Chem.*, 2010, **20**, 2807–2812.

17 Z. Wang, J. S. Chen, T. Zhu, S. Madhavi and X. W. Lou, *Chem. Commun.*, 2010, **46**, 6906–6908.

18 L. Fu, H. Liu, H. Zhang, C. Li, T. Zhang, Y. Wu and H. Wu, *J. Power Sources*, 2006, **159**, 219–222.

19 P. Poizot, S. Laruelle, S. Grugeon, L. Dupont and J. Tarascon, *Nature*, 2000, **407**, 496–499.

20 D. Kong, H. Wang, J. J. Cha, M. Pasta, K. J. Koski, J. Yao and Y. Cui, *Nano Lett.*, 2013, **13**, 1341–1347.

21 Y. Feldman, E. Wasserman, D. Srolovitz and R. Tenne, *Science*, 1995, **267**, 222–225.

22 J. Xiao, X. Wang, X. Q. Yang, S. Xun, G. Liu, P. K. Koech, J. Liu and J. P. Lemmon, *Adv. Funct. Mater.*, 2011, **21**, 2840–2846.

23 Y. Shi, Y. Wang, J. I. Wong, A. Y. S. Tan, C.-L. Hsu, L.-J. Li, Y.-C. Lu and H. Y. Yang, *Sci. Rep.*, 2013, **3**, DOI: 10.1038/srep02169.

24 Y. Miki, D. Nakazato, H. Ikuta, T. Uchida and M. Wakihara, *J. Power Sources*, 1995, **54**, 508–510.

25 H. Hwang, H. Kim and J. Cho, *Nano Lett.*, 2011, **11**, 4826–4830.

26 A. Lynden, *J. Mater. Chem.*, 2012, **22**, 12988–12992.

27 U. K. Sen and S. Mitra, *ACS Appl. Mater. Interfaces*, 2013, **5**, 1240–1247.

28 Z. Wang, W. Liu, W. Xiao and X. W. D. Lou, *Energy Environ. Sci.*, 2013, **6**, 87–91.

29 H. Yu, C. Ma, B. Ge, Y. Chen, Z. Xu, C. Zhu, C. Li, Q. Ouyang, P. Gao and J. Li, *Chem. – Eur. J.*, 2013, **19**, 5818–5823.

30 L. Fei, Y. Xu, X. Wu, G. Chen, Y. Li, B. Li, S. Deng, S. Smirnov, H. Fan and H. Luo, *Nanoscale*, 2014, **6**, 3664–3669.

31 X. Zhou, L.-J. Wan and Y.-G. Guo, *Chem. Commun.*, 2013, **49**, 1838–1840.

32 Y.-T. Liu, X.-D. Zhu, Z.-Q. Duan and X.-M. Xie, *Chem. Commun.*, 2013, **49**, 10305–10307.

33 S.-K. Park, S.-H. Yu, S. Woo, J. Ha, J. Shin, Y.-E. Sung and Y. Piao, *CrystEngComm*, 2012, **14**, 8323–8325.

34 K. Chang and W. Chen, *Chem. Commun.*, 2011, **47**, 4252–4254.

35 S. Ding, D. Zhang, J. S. Chen and X. W. D. Lou, *Nanoscale*, 2012, **4**, 95–98.

36 K. Chang and W. Chen, *ACS Nano*, 2011, **5**, 4720–4728.

37 X. Zhou, L.-J. Wan and Y.-G. Guo, *Nanoscale*, 2012, **4**, 5868–5871.

38 S.-K. Park, S.-H. Yu, S. Woo, B. Quan, D.-C. Lee, M. K. Kim, Y.-E. Sung and Y. Piao, *Dalton Trans.*, 2013, **42**, 2399–2405.

39 X. Zhao, C. Hu and M. Cao, *Chem. – Asian J.*, 2013, **8**, 2701–2707.

40 Y. Peng, Z. Meng, C. Zhong, J. Lu, W. Yu, Z. Yang and Y. Qian, *J. Solid State Chem.*, 2001, **159**, 170–173.

41 M. Wang, G. Li, H. Xu, Y. Qian and J. Yang, *ACS Appl. Mater. Interfaces*, 2013, **5**, 1003–1008.

42 K.-K. Liu, W. Zhang, Y.-H. Lee, Y.-C. Lin, M.-T. Chang, C.-Y. Su, C.-S. Chang, H. Li, Y. Shi and H. Zhang, *Nano Lett.*, 2012, **12**, 1538–1544.

43 C. Altavilla, M. Sarno and P. Ciambelli, *Chem. Mater.*, 2011, **23**, 3879–3885.

44 X.-L. Li and Y.-D. Li, *J. Phys. Chem. B*, 2004, **108**, 13893–13900.

45 L. Yang, L. Liu, Y. Zhu, X. Wang and Y. Wu, *J. Mater. Chem.*, 2012, **22**, 13148–13152.

46 B. Hu, L. Mai, W. Chen and F. Yang, *ACS Nano*, 2009, **3**, 478–482.

47 L. Yang, Q. Gao, Y. Tang, Y. Wu and R. Holze, *J. Power Sources*, 2008, **179**, 357–360.

48 J. Kibsgaard, Z. Chen, B. N. Reinecke and T. F. Jaramillo, *Nat. Mater.*, 2012, **11**, 963–969.

49 H. Li, W. Li, L. Ma, W. Chen and J. Wang, *J. Alloys Compd.*, 2009, **471**, 442–447.

50 H. Liu, D. Su, R. Zhou, B. Sun, G. Wang and S. Z. Qiao, *Adv. Energy Mater.*, 2012, **2**, 970–975.

51 S. Ding, J. S. Chen and X. W. D. Lou, *Chem. – Eur. J.*, 2011, **17**, 13142–13145.

52 Q. Wang and J. Li, *J. Phys. Chem. C*, 2007, **111**, 1675–1682.

53 Z. Wang, T. Chen, W. Chen, K. Chang, L. Ma, G. Huang, D. Chen and J. Y. Lee, *J. Mater. Chem. A*, 2013, **1**, 2202–2210.

54 E. Benavente, M. Santa Ana, F. Mendizábal and G. González, *Coord. Chem. Rev.*, 2002, **224**, 87–109.

55 L. Shen, E. Uchaker, X. Zhang and G. Cao, *Adv. Mater.*, 2012, **24**, 6502–6506.

56 J. Maier, *Nat. Mater.*, 2005, **4**, 805–815.

57 J. Xiao, D. Choi, L. Cosimbescu, P. Koech, J. Liu and J. P. Lemmon, *Chem. Mater.*, 2010, **22**, 4522–4524.

58 S. Zhang, K. Xu and T. Jow, *Electrochim. Acta*, 2004, **49**, 1057–1061.

59 M. E. Orazem and B. Tribollet, *Electrochemical impedance spectroscopy*, Wiley-Interscience, 2011.

60 T. Stephenson, Z. Li, B. Olsen and D. Mitlin, *Energy Environ. Sci.*, 2014, **7**, 209–231.

61 G. Du, Z. Guo, S. Wang, R. Zeng, Z. Chen and H. Liu, *Chem. Commun.*, 2010, **46**, 1106–1108.

62 K. Chang, W. Chen, L. Ma, H. Li, H. Li, F. Huang, Z. Xu, Q. Zhang and J.-Y. Lee, *J. Mater. Chem.*, 2011, **21**, 6251–6257.

7872 | *J. Mater. Chem. A*, 2014, **2**, 7862–7872

This journal is © The Royal Society of Chemistry 2014